SARS-CoV-2 causes severe alveolar inflammation and barrier dysfunction

Stefanie Deinhardt-Emmer[1,2 *], Sarah Böttcher[2], Clio Häring[2], Liane Giebeler[2], Andreas Henke[2], Roland Zell[2], Franziska Hornung[1], Christian Brandt[3], Mike Marquet[3], Alexander S. Mosig[4], Mathias W. Pletz[3], Michael Schacke[2], Jürgen Rödel[1], Regine Heller[5], Sandor Nietzsche[6], Bettina Löffler[1], Christina Ehrhardt[2] *

1 Institute of Medical Microbiology, Jena University Hospital, Am Klinikum 1, D-07747 Jena, Germany
2 Section of Experimental Virology, Institute of Medical Microbiology, Jena University Hospital, Hans-Knoell-Str. 2, D-07745, Jena, Germany
3 Institute for Infectious Diseases and Infection Control, Jena University Hospital, Jena, 07747, Germany
4 Institute of Biochemistry, Jena University Hospital, Am Klinikum 1, D-07743 Jena, Germany
5 Institute of Molecular Cell Biology, Center for Molecular Biomedicine (CMB), Jena University Hospital, Hans-Knoell-Str. 2, D-07745, Jena, Germany
6 Center for Electron Microscopy, Jena University Hospital, Ziegelmuehlenweg 1, D-07743 Jena, Germany

* Correspondence: **Dr. Stefanie Deinhardt-Emmer**
Institute of Medical Microbiology,
Jena University Hospital,
Am Klinikum 1,
D-07747 Jena, Germany

Email: stefanie.deinhardt-emmer@med.uni-jena.de
Phone: 0151 58373822
ORCID: 0000-0003-4495-4052

Prof. Dr. Christina Ehrhardt
Section of Experimental Virology
Institute of Medical Microbiology
Jena University Hospital
Hans-Knoell Str. 2
D-07745 Jena
Email: Christina.Ehrhardt@med.uni-jena.de
Phone: 0049-(0)3641-9395700
ORCID: 0000-0002-8879-6087

Short Running Title: SARS-CoV-2 damage alveolar barrier function

ABSTRACT (172):

Infections with SARS-CoV-2 lead to mild to severe coronavirus disease-19 (COVID-19) with systemic symptoms. Although the viral infection originates in the respiratory system, it is unclear how the virus can overcome the alveolar barrier, which is observed in severe COVID-19 disease courses.

To elucidate the viral effects on the barrier integrity and immune reactions, we used mono-cell culture systems and a complex human alveolus-on-a-chip model composed of epithelial, endothelial, and mononuclear cells.

Our data show that SARS-CoV-2 efficiently infected epithelial cells with high viral loads and inflammatory response, including the interferon expression. By contrast, the adjacent endothelial layer was no infected and did neither show productive virus replication or interferon release. With prolonged infection, both cell types are damaged, and the barrier function is deteriorated, allowing the viral particles to overbear.

In our study, we demonstrate that although SARS-CoV-2 is dependent on the epithelium for efficient replication, the neighboring endothelial cells are affected, e.g., by the epithelial cytokine release, which results in the damage of the alveolar barrier function and viral dissemination.

INTRODUCTION

The novel severe acute respiratory syndrome coronavirus (SARS-CoV-2) is a highly pathogenic virus causing severe respiratory infections, described as coronavirus disease-19 (COVID-19) (Bar-On et al., 2020). Patients suffer from various symptoms as fever, cough, breath shortness, headache, muscle aches, and gastrointestinal symptoms. Hallmarks of severe COVID-19 courses are pneumonia, pulmonary edema, acute respiratory distress syndrome (ARDS), and multiple organ failure. In most patients, the disease has a mild course, but in some cases, e.g., elderly with comorbidities, the infection can develop into a life-threatening condition. In particular preexisting lung pathologies and systemic diseases such as diabetes predispose to severe infection courses described by George et al. (2020).

Clinical studies revealed that the virus primarily replicates in the lung, which can cause severe lung damage up to necrotic destruction of large areas of the lung tissue (Carsana et al., 2020). In autopsies of deceased COVID-19 patients, it has been observed that particularly in severe cases viral particles can disseminate throughout the body (Deinhardt-Emmer et al., 2020b; Wichmann et al., 2020). Additionally, systemic complications have been reported, such as the massive release of proinflammatory cytokines and thromboembolic events in various organs (Becker, 2020). Consequently, SARS-CoV-2 is regarded as a pneumotropic virus that infects the patient via the lung but can also cause a systemic infection that affects different organs with a high mortality rate.

Little is known about the initial infection process in the alveolar lung tissue, particularly about mechanisms that destroy the lung and mechanisms that allow the virus to affect different organs in the body. Infection models that closely reflect the patient's situation are mainly lacking in part due to the challenges to infect mice and the difficulty of accessing and analyzing infected human alveolar lung cells. Up to now, SARS-CoV-2 infection models have been mainly performed with human airway (non-alveolar) cells or non-human cell lines that naturally express the ACE2 viral receptor, such as the African Green Monkey Vero 76 cell line (Hoffmann et al., 2020). These cells lack organ- and species-specific characteristics of human lung epithelial cells. For this purpose, cancerous lung epithelial cells (Calu-3 cells), can at least to some extent, reflect the response of the lung epithelium to viral infection (Bestle et al., 2020).

In our study, we present a human-specific *in vitro*, alveolus-on-a-chip model composed of cells of human origin susceptible for a SARS-CoV-2 infection. This model was only recently developed in our lab (Deinhardt-Emmer et al., 2020a). Within the present study, it was modified by using SARS-CoV-2 permissive epithelial cells (Calu-3 cells). The epithelial and vascular (primarily isolated human umbilical vascular endothelial cells; HUVECs) cells were co-cultured with macrophages (primarily isolated peripheral blood mononuclear cells; PBMCs) resembling the human alveolus architecture and function. This composition is not only relevant for the gas exchange but also for an adequate immune response.

We were able to show that SARS-CoV-2 replicates in the epithelial layer while inducing an acute and robust inflammatory response followed by the destruction of

the epithelial layer. Interestingly, in this infection scenario, the endothelial cells were not invaded by SARS-CoV-2 and did not propagate the virus, but nevertheless the epithelial/endothelial barrier integrity was disrupted.

RESULTS

Efficient SARS-CoV-2 isolation from patients and propagation in cell-culture

To gain fully infectious viral particles for our studies, we collected three respiratory specimens from qRT-PCR-proven COVID-19 patients and performed SARS-CoV-2 propagation in cell culture systems (Vero-76 cells). By repeated infection of host cells and viral replication, we were able to isolate high viral titers originating from three different patients. Within our studies, the SARS-CoV-2 isolates SARS-CoV-2/hu/Germany/Jena-vi005159/2020 (5159), SARS-CoV-2/hu/Germany/Jena-vi005187/2020 (5587) and SARS-CoV-2/hu/Germany/Jena-vi005588/2020 (5588) were employed. Sequencing of virus isolates verified that all three viral strains belong to SARS-CoV-2 (species *Severe acute respiratory syndrome-related coronavirus*, genus *Betacoronavirus*) (Gorbalenya et al., 2020). Phylogenetic analysis revealed a close relationship of SARS-CoV-2 to the SARS-related coronaviruses RaTG13, bat-SL-CoVZXC21 and bat-SL-CoVZC45 (Figure 1A). Within the SARS-CoV-2 clade, the sequences of strains 5587 and 5588 exhibit two base substitutions T8,782C (**nsp1ab:** synonymous) and C28,144T (**nsp8:** S84L), which are characteristic of the all strains of lineage L ((Tang et al., 2020) nomenclature) or lineage B ((Rambaut et al., 2020) nomenclature). Accordingly, 5587 and 5588 clustered with lineage L/lineage B strains

in the phylogenetic analysis (Figure 1B). Furthermore, both strains exhibit deletion of **nsp1ab** D448 and two synonymous substitutions (T514C, C5512T). Beside the **nsp8** S84L substitution, strain 5159 has accumulated three additional amino acid substitutions (**S:** D614G, **nsp1ab:** P4715L and **N:** R203K/G204R) which place this virus in lineage B.1.1 according to the proposed SARS-CoV-2 nomenclature of Rambaut et al. (2020) (Figure 1B).

Mono-culture cells can be infected by SARS-CoV-2 and produce replication complexes at ER-derived membranes.

At first, we infected mono-cell culture systems with SARS-CoV-2 and compared the infection rate between Vero-76 cells and Calu-3 cells. It is already well known that Vero-76 cells can be efficiently infected by SARS-CoV-2 (Hoffmann et al., 2020; Shang et al., 2020). Using transmission electron microscopy (TEM), we could demonstrate that Vero-76 cells host and efficiently propagate the virus (Figure 2A). Figure 2A (upper panel) illustrates infected Vero-76 cell containing viral replication organelles. In the lower-left panel, protein accumulation and generation of double-membrane vesicles are visible. In the middle panel, virion assembly in the ER–Golgi-intermediate compartment (ERGIC) and a Golgi complex are imaged containing morphologically complete viral particles. Here, the particles are packed to be transported to the cellular surface for virus release, which is demonstrated in the right panel. Some particles are still attached to the host cell membrane, whereas some viral particles are already fully released. These results indicate that SARS-CoV-2 induces replication complexes at ER-

154 derived membranes, which were already shown for other types of coronaviruses
155 (Stertz et al., 2007) and also confirm the findings for Vero E6 cells (Ogando et al., 2020).
156 To better mimic the situation in the human pulmonary alveoli, we performed the
157 infection in Calu-3 cells. In Figure 2B, immunofluorescence measurements compare
158 infected Vero-76 cells with infected Calu-3 cells. In both cell types, viral particles can
159 be visualized to a similar extent using specific antibodies against SARS-CoV-2 spike
160 proteins. These results are confirmed by western blot analysis, demonstrating
161 increased levels of SARS-CoV-2 spike protein in the cell lysates after 8h and 24h
162 (Figure 2C).

163 Additionally, we could verify progeny virus particles by performing plaque assays
164 from supernatants of both cell types indicating increased replication during ongoing
165 infection (Figure 2D). Measuring viral RNA-loads in different infected host cell types,
166 we found high RNA levels in Vero-76 and Calu-3 cells (Figure S1A). By contrast,
167 HUVEC mono-cell cultures could not be infected by SARS-CoV-2 (Figure S1B).

168 We further analyzed the host response to the infection by measuring the cytokine
169 mRNA expression of Calu-3 cells. 24h post-infection, many inflammatory cytokines
170 were significantly increased compared to control cells (Figure 3). These results reflect
171 the high cytokine levels found in COVID-19 patients (Costela-Ruiz et al., 2020),
172 indicating that infected epithelial cells contribute to the "cytokine storm" in severe
173 COVID-19 cases. Since different cytokines and chemokines are involved in the
174 infection process, a robust immune response has been associated with a severe clinical
175 course (Coperchini et al., 2020). Our results clearly show that the epithelial cell line

Calu-3 can be efficiently infected by SARS-CoV-2, propagates the virus and answer to the viral infection with a strong cytokine release.

SARS-CoV-2 infects epithelial cells within the alveolus-on-a-chip model causing a strong IFN-response

In the next step, we modified our alveolar-on-a-chip model (Deinhardt-Emmer et al., 2020a) by seeding Calu-3 cells on the epithelial side, primarily isolated HUVECs on the endothelial side and integrated PBMCs to represent the immune response. However, macrophages not show an productive viral replication (Yip et al., 2014), they are mainly involved in inflammatory response (Kumar et al., 2020).

The applied system is ventilated and perfused and can be infected with SARS-CoV-2 via the epithelial side. Using the viral particles isolated from the three COVID-19 patients' specimens, an infection by SARS-CoV-2 on the epithelial cells was proven and the viral particles were propagated (Figure 4A). This effect was still visible after 40h post-infection (Figure S2A). In response to the infection the epithelial cells reacted with a robust cytokine response, demonstrated by elevated IFN-levels in the cell culture supernatants of the epithelial side (Figure 4C).

In general, the production of IFN is the most efficient way of fighting viral infections; e.g. secretion of type I IFN (IFN-α/β) exhibits direct antiviral effects by inhibiting viral replication (Thiel and Weber, 2008) among many other interferon effects that promote the immune response to infection (Kindler 2016). Yet, evasion strategies for different

197 types of coronaviruses have been described. The viruses express factors and posses
198 strategies to inhibit IFN induction/expression (Thoms et al., 2020) or IFN signaling or
199 to increase IFN resistance, which is reviewed by E. Kindler et al. (2016). Consequently,
200 SARS-CoV-2 is apparently able to cope with the interferon response of epithelial cells,
201 which is reflected by our measurements, demonstrating efficient viral replication and
202 persistence for up to 40h despite a strong epithelial interferon response (Figure 3 and
203 4).

204 By contrast, we did not detect viral propagation and did not measure an interferon
205 response at the endothelial side of the biochip (Figure 4C). We could not visualize viral
206 components within endothelial cells neither at 28h (Figure 4B) nor at 40h post-infection
207 (Figure S2B) demonstrating that the viral particles do not productively infect
208 endothelial cells in the human alveolus-on-a-chip model. Additionally, endothelial
209 mono-cell culture systems could not be infected by SARS-CoV-2 (Figure S1A, B)
210 confirming the cell-type specificity of the viral pathogens for lung epithelial cells. This
211 is in line with *in vivo* studies that describe only a weak IFN-response in the serum of
212 COVID-patients (Hu et al., 2020). In animal models with mouse-adapted SARS virus a
213 delayed onset of the IFN-response resulting in immune dysregulation was described
214 (Channappanavar et al., 2016). The weak and delayed IFN-levels in the serum are
215 probably due to the host cell specificity of SARS-CoV-2, as lung epithelium represents
216 the main infection focus and endothelial cells are only hardly/not infected.

217 Taken together, these results indicate that endothelial cells of the lung model are not
218 the primary target cells of SARS-CoV-2 which is in agreement with previous studies

(Bar-On et al., 2020). Further, it is in line with the observation that endothelial layer of the alveolar capillaries of deceased COVID-19 patients were still intact but epithelial tissue was found seriously damaged (Deinhardt-Emmer et al., 2020b). Although the mechanism is not clear the increased proinflammatory cytokine release might cause an endothelial dysfunction. In addition to the origin of endothelial cells from different organs, comorbidities like obesity and diabetes might render endothelial cells susceptible to be infected as recently described (Huertas et al., 2020; Pons et al., 2020). There is clinical evidence for severe courses of COVID-19 in particular, when preexisting endothelial damage can be suspected (Varga et al., 2020).

Further studies are required to elaborate the impact of the endothelial phenotype and the infection conditions at which these cells are targeted by SARS-CoV-2. In the model used in this study, the pneumotropic features of SARS-CoV-2 could be confirmed based on viral uptake and replication in epithelial cells accompanied with an interferon response described in previous studies. The viral particles were not transferred to the neighboring endothelial layer, although the cells were co-cultivated in a bioinspired manner to recreate the alveolar structure.

SARS-CoV-2 disrupts the alveolar barrier within the alveolus-on-a-chip model

Next, we analyzed the barrier function of the epithelial-endothelial cell layers in our biochip model. Many clinical case reports and studies describe that critical ill COVID-patients develop severe lung destructions and a systemic sepsis-like syndrome (Ackermann et al., 2020; Gao et al., 2020) that could be partly explained by a disrupted

barrier function in the lung. From the immunofluorescence image (Figure 4), we could observe some destruction of the epithelial or endothelial layer, in particular 40h post-infection (Figure S2). To better visualize the cell-layers during the infection, we performed scanning electron microscopy (SEM) analysis of the surface structures following 28h post-infection. On the epithelial side we found dead cells and remnants attached to the cell layer. Dying cells are identified by shrinking, balling, disruption of the plasma membrane, and the loss of microvilli, which can be observed in the upper and middle panel of the infected cells, but to a much lesser extent in mock-treated cells (Figure 5A, upper panel). Interestingly, at a higher magnification we could display the viral particles on the surface of the dead cells (Figure 5A, lower panel).

It is well known that respiratory viral pathogens induce cell death (including apoptosis) in the respiratory epithelium, such as the influenza virus (Atkin-Smith et al., 2018). Already the 2003 SARS-CoV led to apoptotic cell death induced by membrane proteins via modulation of the Akt-pathway (Chan et al., 2007). Additionally, prolonged stress of the endoplasmic reticulum (ER) was identified as a trigger for apoptosis (Fung and Liu, 2014). Within the recent pandemic, it has been shown that the largest unique open reading frame (ORF) of the SARS-CoV-2 genome ORF3a is associated with a pro-apoptotic activity (Ren et al., 2020). These studies indicate that the induction of an apoptotic process in the course of SARS-CoV2 infection is highly probable.

By contrast, on the endothelial side, we could not observe differences in the morphological appearance between SARS-CoV-2-infected and mock-treated cells.

Here, the cell integrity of the cell layers appeared intact apart from shrinking artefacts due to the drying procedure (Figure 5B). At the high magnification (lower panel) dead cell remnants show granular residues of the cytoplasm indicating the loss of the plasma membrane, but no viral particles could be visualized.

To measure the epithelial and endothelial cell viability we performed LDH-assays on cells grown in the biochip. 28h post-infection we observed in the infected epithelial layer a significantly enhanced release of LDH, whereas SARS-CoV-2 did not induce an enhanced LDH release in endothelial cells (Figure 5D). However, after more extended infection periods (40h; Figure 5D), the barrier function on the endothelial side was also affected. These results suggest that even if the endothelial layer is not infected the cell integrity gets disturbed, most likely by cytokines released by macrophages. In this respect, it is known that high cytokine/interferon levels can induce the disruption of the alveolar barrier function (Broggi et al., 2020; Gustafson et al., 2020; Pelaia et al., 2020).

To further analyze the barrier integrity of the biochip system on a functional level, we performed permeability assays using FITC-dextran to investigate the endothelial and epithelial cell barrier integrity. We were able to show that SARS-CoV-2 significantly increased the tissue permeability with its barrier function severely impaired (Figure 5C). As a consequence of the disrupted barrier, we detected viral particles by performing plaque assays of the cell supernatants in the endothelial chamber at the late time point of 40h (Figure 5E). These results show that endothelial cells are affected

by the viral infection at late time points and that the disturbed cell integrity results in translocation of the viral particles over the alveolar barrier.

DISCUSSION

In this manuscript, we present an *in vitro* human alveolus-on-a-chip model based on human cells that closely mimics alveolar structures and can be efficiently infected by SARS-CoV-2. The epithelial of the alveolar models was demonstrated to be prone to SARS-CoV2 infection and to propagate viral replication with high viral loads. These findings are in line with clinical observations that in lung tissue by far, the highest viral burdens are measured (Carsana et al., 2020). This phenomenon can be explained by the cell tropism of SARS-CoV-2 to airway cells that contribute to the high shedding of viral particles in the respiratory system and the high infectivity of patients via aerosols. Nevertheless, due to the systemic symptoms in severe COVID-patients, it has been discussed, whether other cell types besides the airway epithelium, are targeted by SARS-COV-2, as well. In particular, vascular complications, such as thrombotic events (Helms et al., 2020), could result from the dissemination and propagation of viral particles in the endothelial system. In our model system, we could not confirm viral invasion into endothelial cells, although the cells were cultured in close proximity to the infected epithelium.

Yet, with increased time of infection (40h), the endothelial cells become damaged resulting in a decline in tissue barrier function. This effect is most likely mediated by

the cytokine release of the infected neighboring epithelium. Cytokine release is known to disturb various cellular functions, such as protein biosynthesis and barrier integrity. Many studies reveal that most severe cases of SARS-CoV-2 infections are not only due to enhanced viral burden, but to a large extent due to aberrant immune responses (Broggi et al., 2020).

In our manuscript, we present an infection model that could be further used to study several aspects during the SARS-CoV-2 infection: (i) At first, the cellular interaction can be analyzed in detail with increasing complexity. Here, the interaction between endothelial and epithelial cells, and the role of different immune cells that can be integrated into the biochip could be elaborated. (ii) Another crucial aspect is preexisting damage, such as diabetic vascular changes or inflammatory foci that may promote a COVID-19 infection. These factors can be mimicked in the biochip model to investigate their impact on infection development. (iii) A third important issue are novel therapeutic agents. Antiviral and anti-inflammatory therapies can be tested in the biochip model to obtain initial results on their mode of action.

Consequently, our biochip model represents a valuable tool to study many aspects during COVID-19 infections.

MATERIAL AND METHODS

Virus isolation, propagation and standard plaque-assays. SARS-CoV-2 was isolated from the respiratory specimen of three different patients and named (SARS-CoV-2/hu/Germany/Jena-vi005159/2020 (5159), SARS-CoV-2/hu/Germany/Jena-

vi005187/2020 (5587) and SARS-CoV-2/hu/Germany/Jena-vi005188/2020) (5588) (ethic approvement of the Jena University Hospital, no.: 2018-1263) by using Vero-76 cells. For this, cells were washed 12 h after seeding and infected with 200 µl filtered patient sample (sterilized syringe filter, pore size 0,2 µm) under the addition of Panserin 401 (PanBiotech, Germany). After five days, the cytopathic effect was notable. Then, cells were frozen, centrifuged, and clear supernatants were obtained.

To generate well-defined viral stocks, plaque purification procedures were performed. For this, confluent Vero-76 cell cultures were infected with serial dilutions of virus isolates diluted in EMEM for 60 min at 37°C and 5% CO_2. Thereafter, inoculum was exchanged with 2 ml MEM/BA (medium with 0.2 % BSA) supplemented with 0.9 % agar (Oxoid, Wesel, Germany), 0.01 % DEAE-Dextran (Pharmacia Biotech, Germany) and 0.2% $NaHCO_3$ until plaque formation was observed. Single plaques were marked using inverse microscopy. Contents of these plaques were used to infect confluent Vero-76 cell monolayers in T25 flasks. Cells were incubated at 37°C and 5% CO_2 until pronounced cytopathic effects were visible. Then, cell cultures were frozen again and clear supernatants were obtained. This plaque purification procedure was repeated again. Finally, virus stocks were generated and titrated using plaque assays. For this, Vero-76 cells were seeded in 6-well plates until a 90 % confluency and infected with serial dilutions of the supernatants in PBS/BA (1 mM MgCl2, 0,9 mM CaCl, 0,2 % BSA, 100 U/ml Pen/Strep) for 90 min at 37°C. After aspiration of the inoculum, cells were incubated with 2 ml MEM/BA (medium with 0.2 % BSA) supplemented with 0.9 % agar (Oxoid, Wesel, Germany), 0.01 % DEAE-Dextran (Pharmacia Biotech, Germany)

and 0,2% NaHCO3 at 37°C and 5 % CO_2 for four days. The visualization was performed by the staining with crystal violet solution (0.2 % crystal violet, 20 % ethanol, 3.5 % formaldehyde in water) and the number of infectious particles (plaque-forming units (PFU) ml^{-1}) was determined.

Sequencing and genome reconstruction. Library preparation was performed according to the "nCoV-2019 sequencing protocol" (dx.doi.org/10.17504/protocols.io.bdp7i5rn) from the ARTICnetwork (https://artic.network/ncov-2019). Briefly, viral RNA was isolated for SARS-CoV-2 virus strains 5159, 5587, and 5588 via the QIAmp viral RNA Kit (Qiagen, Hilden, Germany) according to the manufacturers' guide. The cDNA preparation was performed using the SuperScript IV (Thermofisher), followed by a multiplex PCR to generate overlapping 400 nt amplicons using version 3 of the primer set (https://github.com/artic-network/artic-ncov2019/tree/master/primer_schemes/nCoV-2019/V3). After PCR cleanup, library preparation was performed using the Ligation Sequencing Kit (LSK-109, Oxford Nanopore Technologies) and the Native Barcoding Expansion (EXP-NBD104, native Barcoding Kit (Oxford Nanopore Technologies)). Sequencing was performed on a MinION device using an R.9.4.1 flow cell (Oxford Nanopore Technologies). Basecalling and genome reconstruction was performed using poreCov v.0.2 with the default settings (https://github.com/replikation/poreCov).

Cell culture and virus infection. Vero-76 cells were cultured in EMEM with HEPES modification, and 5 mM L-Glutamine. Calu-3 cells were cultured in RPMI-1640 supplemented with 10 % fetal calves' serum (FCS). M199 was purchased from Lonza (Verviers, Belgium), fetal calf serum (FCS), human serum and endothelial growth supplement were from Sigma (Taufkirchen, Germany).

PBMCs were isolated and cultivated as previously described (Deinhardt-Emmer et al., 2020a). Human umbilical vein endothelial cells (HUVEC) were isolated from anonymously acquired human umbilical cords according to the Declaration of Helsinki, "Ethical principles for Medical Research Involving Human Subjects" (1964). After rinsing the cord veins with 0.9 % NaCl, endothelial cells were detached with collagenase (0.01 %, 3 min at 37 °C), suspended in M199/10 % FCS, washed once (500 x g, 6 min) and seeded on a cell culture flask coated with 0.2 % gelatin. 24 h later, full growth medium was added (M199, 17.5 % FCS, 2.5 % human serum, 7.5 µg/ml endothelial mitogen, 7.5 U/ml heparin, 680 µM glutamine, 100 µM vitamin C, 100 U/ml penicillin, 100 µg/ml streptomycin). HUVEC from the second passage were seeded on 30-mm dishes or on 90-mm dishes at a density of 27,500 cells/cm². Experiments were performed 72 h after seeding. For the cultivation of the human alveolus-on-a-chip model we used Calu-3 cells and macrophages at the epithelial side, and HUVECs at the endothelial side. The Multiorgan tissue flow (MOTiF) biochips were manufactured and obtained from microfluid ChipShop GmbH (Jena, Germany), as explained previously (Deinhardt-Emmer et al., 2020a).

For infection of Vero-76 or Calu-3 cells, cells were washed with PBS and either left uninfected (mock) or infected with SARS-CoV-2 with a multiplicity of infection (MOI) of 1 for 120 min in medium (EMEM with HEPES modification and 5 mM L-Glutamine for Vero-76 cells and RPMI 1640 for Calu-3 cells) supplemented with 10 % FCS. Subsequently, supernatants were removed, and cells were supplemented with fresh medium supplemented with 10 % FCS and further incubated for the times indicated at 37°C, 5 % CO_2.

For the infection of the human alveolus-on-a-chip, cells were washed with PBS once, followed by treatment with PBS (mock) at 37°C and RPMI (0.2 % autologous human serum, 1 mM $MgCl_2$, 0.9 mM $CaCl_2$) or infection with SARS-CoV-2 virus (1 MOI). After 90 min incubation cells were washed and supplemented with medium. Afterwards, cells were incubated for the indicated times at 37°C, 5 % CO_2.

Transmission electron microscopy. Confluent monolayers of Vero-76 cells (9 cm petri dishes) were infected with SARS-CoV-2 (isolate 5159) using an MOI of 1. After 24 h, supernatants were removed, and samples were fixed with freshly prepared modified Karnovsky fixative consisting of 4 % w/v paraformaldehyde and 2.5 % v/v glutaraldehyde in 0.1 M sodium cacodylate buffer pH 7.4 for 1h at room temperature. After washing 3 times for 15 min each with 0.1 M sodium cacodylate buffer (pH 7.4) the cells were post-fixed with 2 % w/v osmium tetroxide for 1h at room temperature. Subsequently, the cells were rewashed with 0.1 M sodium cacodylate buffer (pH 7.4), thoroughly scraped off the petri dishes, and pelleted by centrifuging at 600 x g for 10

min. During the following dehydration in ascending ethanol series, post-staining with 1 % w/v uranyl acetate was performed. Afterwards, the pellets were embedded in epoxy resin (Araldite) and ultrathin sectioned (70 nm) using a Leica Ultracut S (Leica, Wetzlar, Germany). Finally, the sections were mounted on filmed Cu grids, post-stained with lead citrate, and studied in a transmission electron microscope (EM 900, Zeiss, Oberkochen, Germany) at 80 kV and magnifications of 3,000x to 85,000x. For image recording, a 2K slow-scan CCD camera (TRS, Moorenweis, Germany) was used.

Immunofluorescence microscopy. Membranes of the human alveolus-on-a-chip were fixed for at least 30 min with 4 % paraformaldehyde at 37°C and permeabilized with 0.1 % saponin buffer for one hour at room temperature. For the alveolus-on-a-chip model the membrane was removed from the chip after fixation and before permeabilization and cut in two halves to analyze either the epithelial or the endothelial side. Infection by SARS-CoV-2 was visualized using mouse anti-SARS-CoV-2 spike (GeneTex; #GTX632604) IgG monoclonal, primary antibodies and AlexaFluor® goat anti-mouse IgG polyclonal antibodies (Dianova; # 115-545-146). The nuclei were stained with bisBenzimide H 33342 trihydrochloride (Hoechst 33342) (Merck; #14533). Rabbit anti-E-cadherin IgG monoclonal (CellSignaling; 3195S) or rabbit anti-VE-cadherin polyclonal, primary antibodies (CellSignaling; 2158S) and Cy5 goat anti-mouse IgG polyclonal antibodies (Dianova; #111-175-144) were used to detect cell borders of Calu-3 or HUVEC cells on the membrane of the alveolus-on-a-chip model, respectively. Primary antibodies were added 1:100, overnight at 4°C.

435 Afterwards, secondary antibodies and Hoechst 33342 were added 1:100 and 1:1000 for
436 1 h, at room temperature and in the dark. Cells and membranes were mounted with
437 fluorescence mounting media (Dako; #S3023).
438 Images were acquired using an Axio Observer.Z1 microscope (Zeiss) with Plan
439 Apochromat 20x/0.8 objective (Zeiss), ApoTome.2 (Zeiss) and Axiocam 503 mono
440 (Zeiss) and the software Zen 2.6 (blue edition; Zeiss). Apotome defolding with phase
441 error correction and deconvolution was done by the software Zen 2.6 as well. Fiji V
442 1.52b (ImageJ) was used for further image processing, including Z-stack merging with
443 maximum intensity projection and gamma correction. Parameters were kept the same
444 for all pictures which were compared with each other.
445
446 **Scanning electron microscopy.** The fixation of the cells was performed inside the
447 human alveolus-on-a-chip model by using the same fixative as for TEM for 60 min at
448 room temperature as described previously (Deinhardt-Emmer et al., 2020a; Maurer et
449 al., 2019; Rennert et al., 2015). Afterwards, the chips were rinsed three times with fresh
450 cacodylate buffer for 10 min each and the membranes were cut out. After post-fixation
451 with 2 % w/v osmiumtetroxide for 1h the samples were dehydrated in ascending
452 ethanol concentrations (30, 50, 70, 90 and 100 %) for 15 min each. Subsequently, the
453 samples were critical-point dried using liquid CO_2 and sputter coated with gold
454 (thickness approx. 2 nm) using a CCU-010 sputter coater (safematic GmbH, Zizers,
455 Switzerland). The specimens were investigated with a field emission SEM LEO-1530
456 Gemini (Carl Zeiss NTS GmbH, Oberkochen, Germany).

457

458 **Western-Blot Analysis.** For western blotting, cells were lysed with Triton lysis buffer
459 (TLB; 20 mM Tris-HCl, pH 7.4; 137 mM NaCl; 10% Glycerol; 1% Triton X-100; 2
460 mM EDTA; 50 mM sodium glycerophosphate, 20 mM sodium pyrophosphate; 5
461 µg ml^{-1} aprotinin; 5 µg ml^{-1} leupeptin; 1 mM sodium vanadate and 5 mM
462 benzamidine) for 30 min. Cell lysates were cleared by centrifugation, supplemented
463 with 5x Lämmli buffer (10% SDS, 50% glycerol, 25% 2-mercaptoethanol, 0.02%
464 bromophenol blue, 312 mM Tris 6.8 pH) (diluted 1:5), boiled for 10 min (95°C), and
465 subjected to SDS-PAGE and subsequent blotting. For the detection of SARS-CoV-2
466 spike protein a rabbit polyclonal anti-SARS-CoV-2 spike S2 antibody (Sino Biological
467 #40590-T62) was used.

468

469 **Lactate Dehydrogenase Cytotoxicity Assay.** Cell cytotoxicity was determined with
470 CyQUANT Lactate Dehydrogenase (LDH) Cytotoxicity Assay Kit (Invitrogen/Thermo
471 Fisher Scientific,Waltham, USA) according to the manufacturer´s instructions. Cells
472 were infected as previously described. After infection 25 µl of the supernatant was
473 transferred in technical duplicates to a 96-well plate and mixed with 25 µl of the LDH
474 cytotoxicity assay reagent. The plate was incubated at 37°C for 30 min. Stop-Solution
475 (25 µl) was added, and OD_{492nm} was directly measured using a TECAN Spectra fluor
476 plate reader (Tecan Group Ltd, Maennedorf, Switzerland). The OD_{620nm} was subtracted
477 to correct for background signal.

478

Permeability Assay. To test the permeability of the epithelial and endothelial barrier, 1 mg ml^{-1} of 3–5 kDa fluorescein isothio-cyanate (FITC)-dextran (Sigma-Aldrich, Germany) in phenol-red free DMEM/F12 medium (Sigma-Aldrich, Germany) was injected into the upper chamber of the chip. The lower chamber contained only phenol red free DMEM/F12. The alveolus model was incubated for 60 min under static conditions. Afterwards, the media from the lower and upper chambers were collected, and fluorescence intensity (exc. 488nm; em. 518 nm) was measured in a 96-well μClear black plate (Greiner BioOne, Frickenhausen, Germany) by a BMG Labtech FLUOStar Omega microplate reader (BMG Labtech GmbH, Ortenberg, Germany). The permeability coefficient (P_{app}) was calculated according to P_{app} (cm s^{-1}) = (dQ/dt) (1/AC_o). For this, dQ/dt represent the steady-state flux (g s^{-1}), A the culture surface area (cm^2) and C_o the initial concentration (mg ml^{-1}) (Thomas et al., 2017).

Detection of mRNA-expression by using qRT-PCR. For RNA isolation cells were lysed with 350 µl RLT lysis buffer and detached from the plate using a rubber cell scraper. RNA isolation was performed using the RNeasy Mini Kit (QIAGEN, Hilden, Germany) according to the manufacturer's protocol. RNA concentration was measured using the Nano Drop Spectrophotometer ND-1000 (preqlab/vwr, Radnor, USA).

For cDNA synthesis, the QuantiNova Reverse Transcription Kit (QIAGEN, Venlo, Netherlands) was used. RNA was thawed on ice. 400 nanogram (ng) RNA were diluted in RNase free water to a volume of 13 µl. 2 µl gDNA removal mix were added

501 to the diluted RNA; followed by incubation at 45°C for 2 min. After incubating the
502 samples for at least 1 min on ice, 5 µl of RT master mix (containing 4 µl Reverse
503 Transcription Mix and 1 µl Reverse Transcription enzyme per sample) were added.
504 The resulting mixture was incubated for 3 min at 25°C, followed by incubation at 45°C
505 for 10 min and an inactivation step at 85°C for 5 min. The cDNA was either directly
506 used for the subsequent experiments or stored at -20°C.
507 qRT-PCRs were performed using the QuantiNova SYBR Green PCR Kit (QIAGEN,
508 Venlo, Netherlands). 1 µl cDNA was added to 19 µl master mix (containing 10 µl SYBR
509 Green, 1.5 µl Forward Primer (10 µM), 1.5 µl Reverse Primer (10 µM) and 6 µL RNase
510 free ddH_2O per sample; for primer sequences see table 1), and the real time PCR
511 reaction was started using the following cycle conditions: 95l°C for 2 min, followed by
512 40 cycles of 95°C for 5 sec and 60°C for 10 sec. The qPCR cycle was ended by a stepwise
513 temperature-increase from 60°C to 95°C (1°C every 5 sec).
514
515 **Detection of SARS-CoV-2 by using qRT-PCR.** For the determination of SARS-CoV-
516 2, we used the QIAamp Viral RNA Mini Kit (Qiagen, Hilden, Germany) according to
517 manufacturer's guide. A qRT-PCR from RIDAgene (r-biopharm, Darmstadt,
518 Germany) followed on Rotor-Gene Q (Qiagen, Hilden, Germany) to detect the E-gene
519 of SARS-CoV-2. The RNA standard curve, prepared from the positive control of the
520 RIDAgene (r-biopharm, Darmstadt, Germany) kit, Cycle conditions were set as
521 follows: 10 min at 58°C, 1 min at 95°C and 45 cycles of 95°C for 15 sec and 60°C for 30
522 sec.

Statistical analysis. Statistical analyses were performed using Prism 8 (GraphPad Software). Statistical methods are described in the figure legends.

Funding

The authors acknowledge the support by grants of the BMBF (01KI20168) and the Carl Zeiss Foundation. The authors further acknowledge the support of this work by a grant from the IZKF (ACSP02) (SDE). The study was further funded by the Deutsche Forschungsgemeinschaft (DFG, German Research Foundation) under Germany´s Excellence Strategy – EXC 2051 – Project-ID 390713860. We acknowledge support by the German Research Foundation and the Open Acess Publication Fund of the Thueringer Universitaets- und Landesbibliothek Jena Projekt Nr. 433052568.

Author contributions. SDE, BL and CE conceived and designed the experiments, SDE, SB, CH, LG, AH, RZ, FH, CB, MM, MS, and SN performed the experiments**,** SDE, SB, CH, LG, RZ, ASM, CB, SN, BL and CE analyzed the data, SDE, BL and CE wrote the manuscript, SDE, ASM, MWP, RH, SN, BL and CE provided resources. All authors critically read and commented on the manuscript.

Acknowledgments

We thank the team at the Placenta Laboratory of the Jena University Hospital for supplying umbilical cords for HUVEC isolation and the excellent technical work of

Elke Teuscher regarding the preparation. Furthermore, we thank Stefanie Kynast for the excellent cell cultivation and laboratory assistance. The authors also thank Anika Hopf (Center for Electron Microscopy) for her excellent work in sample preparation.

References

Ackermann, M., S.E. Verleden, M. Kuehnel, A. Haverich, T. Welte, F. Laenger, A. Vanstapel, C. Werlein, H. Stark, A. Tzankov, W.W. Li, V.W. Li, S.J. Mentzer, and D. Jonigk. 2020. Pulmonary Vascular Endothelialitis, Thrombosis, and Angiogenesis in Covid-19. *New England Journal of Medicine* 383:120-128.

Atkin-Smith, G.K., M. Duan, W. Chen, and I.K.H. Poon. 2018. The induction and consequences of Influenza A virus-induced cell death. *Cell Death & Disease* 9:1002.

Bar-On, Y.M., A. Flamholz, R. Phillips, and R. Milo. 2020. SARS-CoV-2 (COVID-19) by the numbers. *eLife* 9:e57309.

Becker, R.C. 2020. COVID-19 update: Covid-19-associated coagulopathy. *J Thromb Thrombolysis* 50:54-67.

Bestle, D., M.R. Heindl, H. Limburg, T. Van Lam van, O. Pilgram, H. Moulton, D.A. Stein, K. Hardes, M. Eickmann, O. Dolnik, C. Rohde, H.D. Klenk, W. Garten, T. Steinmetzer, and E. Böttcher-Friebertshäuser. 2020. TMPRSS2 and furin are both essential for proteolytic activation of SARS-CoV-2 in human airway cells. *Life Sci Alliance* 3:

Broggi, A., S. Ghosh, B. Sposito, R. Spreafico, F. Balzarini, A. Lo Cascio, N. Clementi, M. De Santis, N. Mancini, F. Granucci, and I. Zanoni. 2020. Type III interferons disrupt the lung epithelial barrier upon viral recognition. *Science (New York, N.Y.)*

Carsana, L., A. Sonzogni, A. Nasr, R.S. Rossi, A. Pellegrinelli, P. Zerbi, R. Rech, R. Colombo, S. Antinori, M. Corbellino, M. Galli, E. Catena, A. Tosoni, A. Gianatti, and M. Nebuloni. 2020. Pulmonary post-mortem findings in a series of COVID-19 cases from northern Italy: a two-centre descriptive study. *The Lancet Infectious Diseases*

Chan, C.-M., C.-W. Ma, W.-Y. Chan, and H.Y.E. Chan. 2007. The SARS-Coronavirus Membrane protein induces apoptosis through modulating the Akt survival pathway. *Arch Biochem Biophys* 459:197-207.

Channappanavar, R., A.R. Fehr, R. Vijay, M. Mack, J. Zhao, D.K. Meyerholz, and S. Perlman. 2016. Dysregulated Type I Interferon and Inflammatory Monocyte-Macrophage Responses Cause Lethal Pneumonia in SARS-CoV-Infected Mice. *Cell Host Microbe* 19:181-193.

Coperchini, F., L. Chiovato, L. Croce, F. Magri, and M. Rotondi. 2020. The cytokine storm in COVID-19: An overview of the involvement of the chemokine/chemokine-receptor system. *Cytokine Growth Factor Rev* 53:25-32.

Costela-Ruiz, V.J., R. Illescas-Montes, J.M. Puerta-Puerta, C. Ruiz, and L. Melguizo-Rodríguez. 2020. SARS-CoV-2 infection: The role of cytokines in COVID-19 disease. *Cytokine Growth Factor Rev* S1359-6101(1320)30109-X.

Deinhardt-Emmer, S., K. Rennert, E. Schicke, Z. Cseresnyés, M. Windolph, S. Nietzsche, R. Heller, F. Siwczak, K.F. Haupt, S. Carlstedt, M. Schacke, M.T. Figge, C. Ehrhardt, B. Löffler, and A.S. Mosig. 2020a. Co-infection with Staphylococcus aureus after primary influenza virus infection leads to damage of the endothelium in a human alveolus-on-a-chip model. *Biofabrication* 12:025012.

588 Deinhardt-Emmer, S., D. Wittschieber, J. Sanft, S. Kleemann, S. Elschner, K.F. Haupt, V. Vau,
589 C. Häring, J. Rödel, A. Henke, C. Ehrhardt, M. Bauer, M. Philipp, N. Gaßler, S.
590 Nietzsche, B. Löffler, and G. Mall. 2020b. Early postmortem mapping of SARS-CoV-2
591 RNA in patients with COVID-19 and correlation to tissue damage. *bioRxiv*
592 2020.2007.2001.182550.
593 Fung, T.S., and D.X. Liu. 2014. Coronavirus infection, ER stress, apoptosis and innate
594 immunity. *Front Microbiol* 5:
595 Gao, Y.M., G. Xu, B. Wang, and B.C. Liu. 2020. Cytokine storm syndrome in coronavirus
596 disease 2019: A narrative review. *J Intern Med*
597 George, P.M., A.U. Wells, and R.G. Jenkins. 2020. Pulmonary fibrosis and COVID-19: the
598 potential role for antifibrotic therapy. *The Lancet Respiratory Medicine*
599 Gorbalenya, A.E., S.C. Baker, R.S. Baric, R.J. de Groot, C. Drosten, A.A. Gulyaeva, B.L.
600 Haagmans, C. Lauber, A.M. Leontovich, B.W. Neuman, D. Penzar, S. Perlman, L.L.M.
601 Poon, D.V. Samborskiy, I.A. Sidorov, I. Sola, J. Ziebuhr, and V. Coronaviridae Study
602 Group of the International Committee on Taxonomy of. 2020. The species Severe
603 acute respiratory syndrome-related coronavirus: classifying 2019-nCoV and naming it
604 SARS-CoV-2. *Nature microbiology* 5:536-544.
605 Gustafson, D., S. Raju, R. Wu, C. Ching, S. Veitch, K. Rathnakumar, E. Boudreau, K.L. Howe,
606 and J.E. Fish. 2020. Overcoming Barriers: The Endothelium As a Linchpin of
607 Coronavirus Disease 2019 Pathogenesis? *Arterioscler Thromb Vasc Biol* 40:1818-
608 1829.
609 Helms, J., C. Tacquard, F. Severac, I. Leonard-Lorant, M. Ohana, X. Delabranche, H. Merdji, R.
610 Clere-Jehl, M. Schenck, F. Fagot Gandet, S. Fafi-Kremer, V. Castelain, F. Schneider, L.
611 Grunebaum, E. Anglés-Cano, L. Sattler, P.-M. Mertes, F. Meziani, and C.T. Group.
612 2020. High risk of thrombosis in patients with severe SARS-CoV-2 infection: a
613 multicenter prospective cohort study. *Intensive Care Med* 46:1089-1098.
614 Hoffmann, M., H. Kleine-Weber, S. Schroeder, N. Krüger, T. Herrler, S. Erichsen, T.S.
615 Schiergens, G. Herrler, N.H. Wu, A. Nitsche, M.A. Müller, C. Drosten, and S.
616 Pöhlmann. 2020. SARS-CoV-2 Cell Entry Depends on ACE2 and TMPRSS2 and Is
617 Blocked by a Clinically Proven Protease Inhibitor. *Cell* 181:271-280.e278.
618 Hu, B., S. Huang, and L. Yin. 2020. The cytokine storm and COVID-19. *Journal of Medical*
619 *Virology* n/a:
620 Huertas, A., D. Montani, L. Savale, J. Pichon, L. Tu, F. Parent, C. Guignabert, and M. Humbert.
621 2020. Endothelial cell dysfunction: a major player in SARS-CoV-2 infection (COVID-
622 19)? *European Respiratory Journal* 2001634.
623 Kumar, S., R. Nyodu, V.K. Maurya, and S.K. Saxena. 2020. Host Immune Response and
624 Immunobiology of Human SARS-CoV-2 Infection. *Coronavirus Disease 2019 (COVID-*
625 *19)* 43-53.
626 Maurer, M., M.S. Gresnigt, A. Last, T. Wollny, F. Berlinghof, R. Pospich, Z. Cseresnyes, A.
627 Medyukhina, K. Graf, M. Gröger, M. Raasch, F. Siwczak, S. Nietzsche, I.D. Jacobsen,
628 M.T. Figge, B. Hube, O. Huber, and A.S. Mosig. 2019. A three-dimensional
629 immunocompetent intestine-on-chip model as in vitro platform for functional and
630 microbial interaction studies. *Biomaterials* 220:119396.
631 Ogando, N.S., T.J. Dalebout, J.C. Zevenhoven-Dobbe, R.W. Limpens, Y. van der Meer, L. Caly,
632 J. Druce, J.J.C. de Vries, M. Kikkert, M. Bárcena, I. Sidorov, and E.J. Snijder. 2020.
633 SARS-coronavirus-2 replication in Vero E6 cells: replication kinetics, rapid adaptation
634 and cytopathology. *bioRxiv* 2020.2004.2020.049924.

635 Pelaia, C., C. Tinello, A. Vatrella, G. De Sarro, and G. Pelaia. 2020. Lung under attack by
636 COVID-19-induced cytokine storm: pathogenic mechanisms and therapeutic
637 implications. *Ther Adv Respir Dis* 14:1753466620933508.
638 Pons, S., S. Fodil, E. Azoulay, and L. Zafrani. 2020. The vascular endothelium: the cornerstone
639 of organ dysfunction in severe SARS-CoV-2 infection. *Crit Care* 24:353-353.
640 Rambaut, A., E.C. Holmes, Á. O'Toole, V. Hill, J.T. McCrone, C. Ruis, L. du Plessis, and O.G.
641 Pybus. 2020. A dynamic nomenclature proposal for SARS-CoV-2 lineages to assist
642 genomic epidemiology. *Nature microbiology*
643 Ren, Y., T. Shu, D. Wu, J. Mu, C. Wang, M. Huang, Y. Han, X.-Y. Zhang, W. Zhou, Y. Qiu, and X.
644 Zhou. 2020. The ORF3a protein of SARS-CoV-2 induces apoptosis in cells. *Cellular &*
645 *Molecular Immunology*
646 Rennert, K., S. Steinborn, M. Gröger, B. Ungerböck, A.M. Jank, J. Ehgartner, S. Nietzsche, J.
647 Dinger, M. Kiehntopf, H. Funke, F.T. Peters, A. Lupp, C. Gärtner, T. Mayr, M. Bauer, O.
648 Huber, and A.S. Mosig. 2015. A microfluidically perfused three dimensional human
649 liver model. *Biomaterials* 71:119-131.
650 Shang, J., Y. Wan, C. Luo, G. Ye, Q. Geng, A. Auerbach, and F. Li. 2020. Cell entry mechanisms
651 of SARS-CoV-2. *Proceedings of the National Academy of Sciences* 117:11727.
652 Stertz, S., M. Reichelt, M. Spiegel, T. Kuri, L. Martínez-Sobrido, A. García-Sastre, F. Weber,
653 and G. Kochs. 2007. The intracellular sites of early replication and budding of SARS-
654 coronavirus. *Virology* 361:304-315.
655 Tang, X., C. Wu, X. Li, Y. Song, X. Yao, X. Wu, Y. Duan, H. Zhang, Y. Wang, Z. Qian, J. Cui, and J.
656 Lu. 2020. On the origin and continuing evolution of SARS-CoV-2. *National Science*
657 *Review* 7:1012-1023.
658 Thiel, V., and F. Weber. 2008. Interferon and cytokine responses to SARS-coronavirus
659 infection. *Cytokine Growth Factor Rev* 19:121-132.
660 Thomas, L., Z. Rao, J. Gerstmeier, M. Raasch, C. Weinigel, S. Rummler, D. Menche, R. Muller,
661 C. Pergola, A. Mosig, and O. Werz. 2017. Selective upregulation of TNFalpha
662 expression in classically-activated human monocyte-derived macrophages (M1)
663 through pharmacological interference with V-ATPase. *Biochemical pharmacology*
664 130:71-82.
665 Thoms, M., R. Buschauer, M. Ameismeier, L. Koepke, T. Denk, M. Hirschenberger, H. Kratzat,
666 M. Hayn, T. Mackens-Kiani, J. Cheng, J.H. Straub, C.M. Stürzel, T. Fröhlich, O.
667 Berninghausen, T. Becker, F. Kirchhoff, K.M.J. Sparrer, and R. Beckmann. 2020.
668 Structural basis for translational shutdown and immune evasion by the Nsp1 protein
669 of SARS-CoV-2. *Science (New York, N.Y.)* eabc8665.
670 Varga, Z., A.J. Flammer, P. Steiger, M. Haberecker, R. Andermatt, A.S. Zinkernagel, M.R.
671 Mehra, R.A. Schuepbach, F. Ruschitzka, and H. Moch. 2020. Endothelial cell infection
672 and endotheliitis in COVID-19. *The Lancet* 395:1417-1418.
673 Wichmann, D., J.-P. Sperhake, M. Lütgehetmann, S. Steurer, C. Edler, A. Heinemann, F.
674 Heinrich, H. Mushumba, I. Kniep, A.S. Schröder, C. Burdelski, G. de Heer, A. Nierhaus,
675 D. Frings, S. Pfefferle, H. Becker, H. Bredereke-Wiedling, A. de Weerth, H.-R. Paschen,
676 S. Sheikhzadeh-Eggers, A. Stang, S. Schmiedel, C. Bokemeyer, M.M. Addo, M.
677 Aepfelbacher, K. Püschel, and S. Kluge. 2020. Autopsy Findings and Venous
678 Thromboembolism in Patients With COVID-19. *Annals of Internal Medicine*
679 Yip, M.S., N.H.L. Leung, C.Y. Cheung, P.H. Li, H.H.Y. Lee, M. Daëron, J.S.M. Peiris, R. Bruzzone,
680 and M. Jaume. 2014. Antibody-dependent infection of human macrophages by
681 severe acute respiratory syndrome coronavirus. *Virol J* 11:82-82.
682

683
684
685
686
687
688
689
690

691 **Figure legends**

692 **Figure 1: Phylogenetic tree of SARS-CoV-2.**

693 (A) Phylogenetic analysis revealed a close relationship of SARS-CoV-2 to the SARS-
694 related coronaviruses RaTG13, bat-SL-CoVZXC21 and bat-SL-CoVZC45. Sequences of
695 strains 5587 and 5588 exhibit two base substitutions T8,782C (**nsp1ab:** synonymous)
696 and C28,144T (**nsp8:** S84L). (B) Accordingly, 5587 and 5588 clustered with lineage
697 L/lineage B strains in the phylogenetic analysis. Both strains exhibit deletion of **nsp1ab**
698 D448 and two synonymous substitutions (T514C, C5512T). Beside the **nsp8** S84L
699 substitution, strain 5159 has accumulated three additional amino acid substitutions (**S:**
700 D614G, **nsp1ab:** P4715L and **N:** R203K/G204R) which place this virus in lineage B.1.1.

701

702 **Figure 2: SARS-CoV-2 replicates in Vero-76 and Calu-3 cells.**

703 Vero-76 (A-D) and Calu-3 (B-D) cells were left uninfected (mock) (B-D) or were
704 infected (A-D) with a SARS-CoV-2 patient isolate (5159) (MOI=1).

705 (A) Transmission electron microscopy was performed 24h post infection (p.i.): (upper
706 panel, scale bar: 5 µm) overview of 3 SARS-CoV-2-infected Vero-76 cells; (lower left
707 panel, scale bar: 200 nm) generation of double membrane vesicles; (lower middle
708 panel, scale bar: 200 nm) virion assembly in the ER–Golgi-intermediate compartment

(ERGIC); (lower right panel, scale bar: 200 nm) viral release. (B) SARS-CoV-2 was visualized by detection of the spike protein via a spike-specific antibody and an Alexa Fluor™ 488-conjugated goat anti-mouse IgG (green). The nuclei were stained with Hoechst 33342 (blue). Immunofluorescence (IF) microscopy was acquired by use of the Axio Observer.Z1 (Zeiss) with a 200×magnification. (C) Total cell lysates were harvested at the times indicated and expression of the spike protein was analyzed by western-blot assay. ERK2 served as loading control. (D) Progeny virus particles were measured in the supernatant by standard plaque assay at the indicated times post infection. Shown are means (±SD) of plaque forming units (PFU) ml^{-1} of three independent experiments including two biological samples. Statistical significance was analyzed by unpaired, two-tailed t-test (***$p < 0.001$).

Figure 3: SARS-CoV-2 infection results in induction of antiviral and proinflammatory mRNA synthesis.

Calu-3 cells were left uninfected (mock) or were infected with a SARS-CoV-2 patient isolate (5159, 5587, 5588) (MOI=1). RNA-lysates were performed 24h p.i. Levels of IFNα, IFNβ, IFNλ1, IFNλ2,3, IL6, IL8, IP10, TNFα, cIAP2, TRAIL, and RIPK1 mRNA were measured of three patient isolate (5159, 5587, 5588) and two technical samples in 3 independent experiments. Means ± SD of three independent experiments are shown. Levels of mock-treated samples were arbitrarily set as 1. After normalization, two-tailed unpaired t-tests were performed for comparison of mock-treated and SARS-CoV-2-infected and samples. (*$p < 0.05$, **$p < 0.01$, ***$p < 0.001$, ****$p < 0.0001$).

Figure 4: SARS-CoV-2 efficiently infects epithelial cells of the human-alveolus-on-a chip model and provokes type I and III interferon production.

(A-C) The epithelial chamber of the alveolus-on-a-chip model was left uninfected (mock) or infected with three different SARS-CoV-2 patient isolates (5159, 5587, 5588) (MOI=1). (A, B) Immunofluorescence staining was performed 28h p.i. and analyzed by immunofluorescence microscopy (Axio Observer.Z1 (Zeiss)). (A) The E-cadherin of the epithelial layer and the (B) VE-cadherin of the endothelial layer were visualized by an anti-E-Cadherin-specific antibody or an anti-VE-Cadherin antiserum, respectively, and a Cy5 goat anti-rabbit IgG (red). (A, B) The SARS-CoV-2 was visualized by detection of the spike protein via a spike-specific antibody and an Alexa Fluor™ 488-conjugated goat anti-mouse IgG (green). The nuclei were stained with Hoechst 33342 (blue). Scale bars represent 100 μm. (C) Production of antiviral cytokines derived from the epithelial side was determined by use of Legendplex Panel (Biolegend, CA, USA). SARS-CoV-2 induced IFNβ, IFNλ1 and IFNλ2,3 release (pg/ml) was measured. Means ± SD of three independent experiments each infected with another patient isolate (5159, 5587, 5588) are shown. Levels of mock-treated samples were arbitrarily set as 1. After normalization, two-tailed unpaired t-tests were performed for comparison of mock-treated and SARS-CoV-2-infected and samples. (**$p < 0.01$).

Figure 5: SARS-CoV-2 infection results in the disruption of barrier integrity in the human-alveolus-on-a chip model.

753 The epithelial side of the alveolus-on-a-chip model was left uninfected (mock) or
754 infected with the SARS-CoV-2 patient isolate (5159) (MOI=1) for 28h. An overview
755 (upper panel) of the (A) epithelial layer and (B) endothelial layer are depicted. Dead
756 cells (middle panel) are focused. The surface of dead cells (lower panel) shows
757 particles (arrows) attached to the plasma membranes of the epithelial cells only. Scale
758 bars represent 50 µm (200×magnification), 5 µm (2.000×magnification) and 200 nm
759 (60.000×magnification).
760 (C) Barrier function of the human alveolus-on-a-chip model was analyzed by a
761 permeability assay of mock-infected and SARS-CoV-2-infected human alveolus-on-a-
762 chip model using FITC-dextran at 28h p.i., FITC-dextran was measured via the
763 fluorescence intensity (exc. 488nm; em. 518 nm) and depicted as the permeability
764 coefficient (P_{app}), calculated according to P_{app} (cm s^{-1}) = (dQ/dt) (1/AC_o). Results show
765 significant higher barrier permeability after SARS-CoV-2 infection. (D) Supernatants
766 of the epithelial- and endothelial side of SARS-CoV-2 infected human alveolus-on-a-
767 chip models were used to perform LDH-assays indicating cell membrane rupture at
768 28h and 40h p.i.. (E) Progeny virus titers were analyzed in the supernatants of the
769 epithelial- and endothelial layer by standard plaque assay.
770 Shown are means (±SD) of (C) three independent experiments each infected with
771 another patient isolate (5159, 5587, 5588), (D) LDH release, and (E) plaque forming
772 units (PFU/ml). Statistical significance was analyzed by unpaired, two-tailed t-test (*p
773 < 0.05, **p < 0.01).
774

Figure S1: SARS-CoV-2 infects epithelial cells productively.

(A) Vero-76, Calu-3, and HUVECs were infected with a SARS-CoV-2 patient isolate (5159, 5587, 5588) (MOI=1). RNA-lysates were performed 24h p.i. and copies of viral RNA (E-gene) were determined by r-biopharm qRT-PCR. Means ± SD of three independent experiments are shown.

(B) HUVECs were infected with a SARS-CoV-2 patient isolate (5159) (MOI=1) for 4h, 8h, and 24h. SARS-CoV-2 was visualized by detection of the spike protein via a spike-specific antibody and an Alexa Fluor™ 488-conjugated goat anti-mouse IgG (green). The nuclei were stained with Hoechst 33342 (blue). Immunofluorescence (IF) microscopy was acquired by use of the Axio Observer.Z1 (Zeiss) with a 200×magnification.

Figure S2: Infection with SARS-CoV-2 results in the disruption of the epithelial- and endothelial barrier.

The epithelial side of the alveolus-on-a-chip model was left uninfected (mock) or infected with three different SARS-CoV-2 patient isolates (5159, 5587, 5588) (MOI=1). Immunofluorescence staining was performed 40h p.i., (A) The E-cadherin of the epithelial layer and the (B) VE-cadherin of the endothelial layer were visualized by an anti-E-Cadherin-specific antibody or an anti-VE-Cadherin antiserum, respectively, and a Cy5 goat anti-rabbit IgG (red). (A, B) The SARS-CoV-2 was visualized by detection of the spike protein via a spike-specific antibody and an Alexa Fluor™ 488-

conjugated goat anti-mouse IgG (green). The nuclei were stained with Hoechst 33342 (blue). Scale bars represent 100 μm.

Figure 1

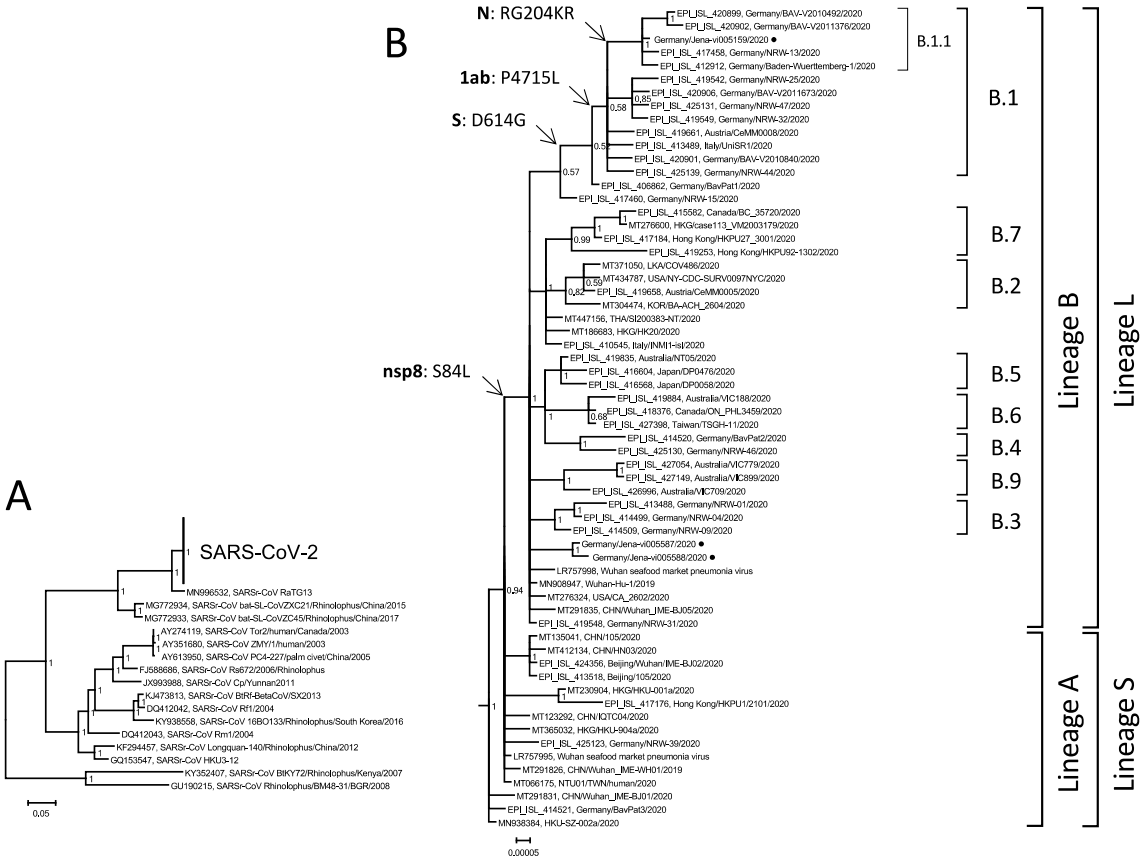

798

799

Figure 2

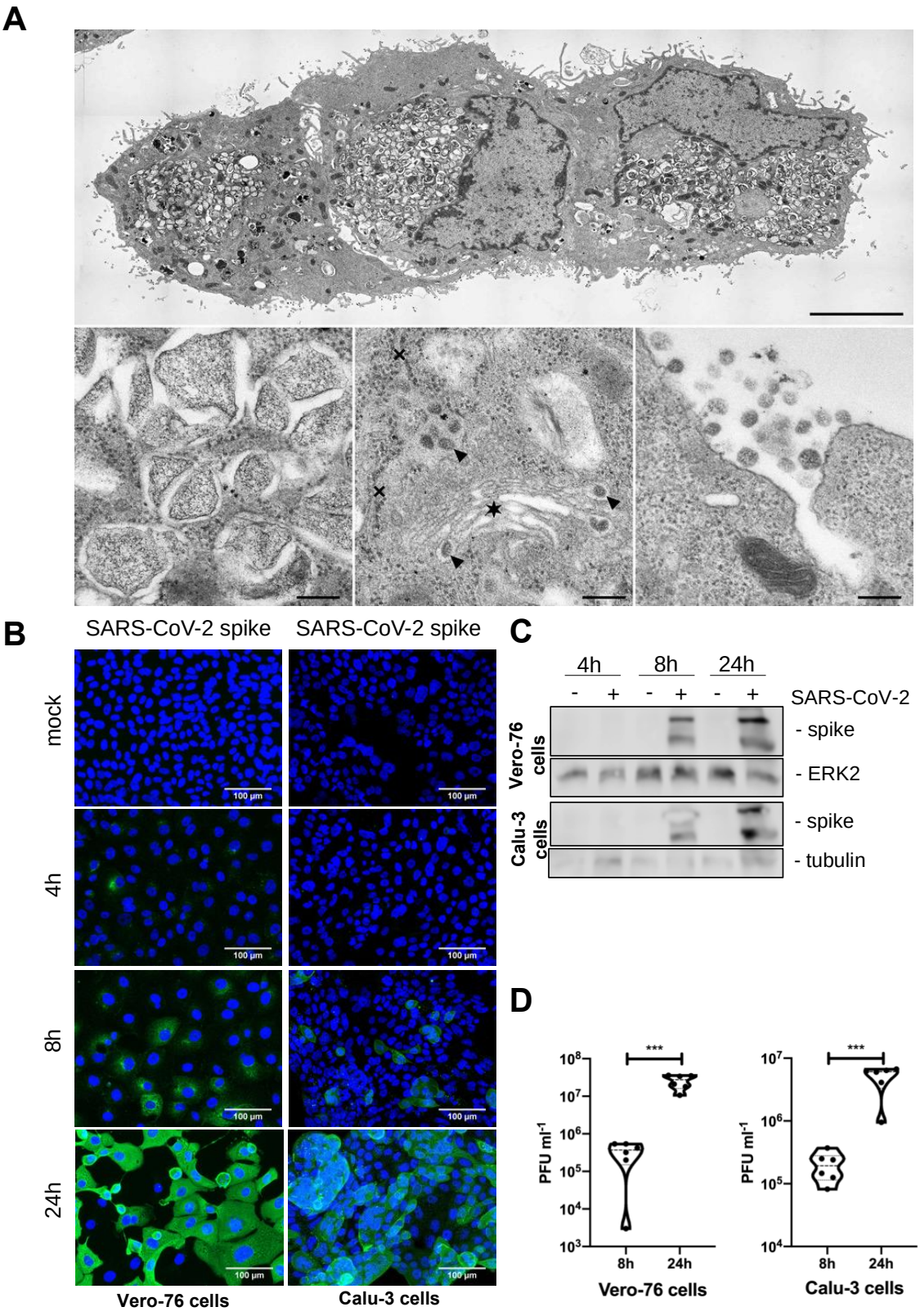

800

801

Figure 3

A

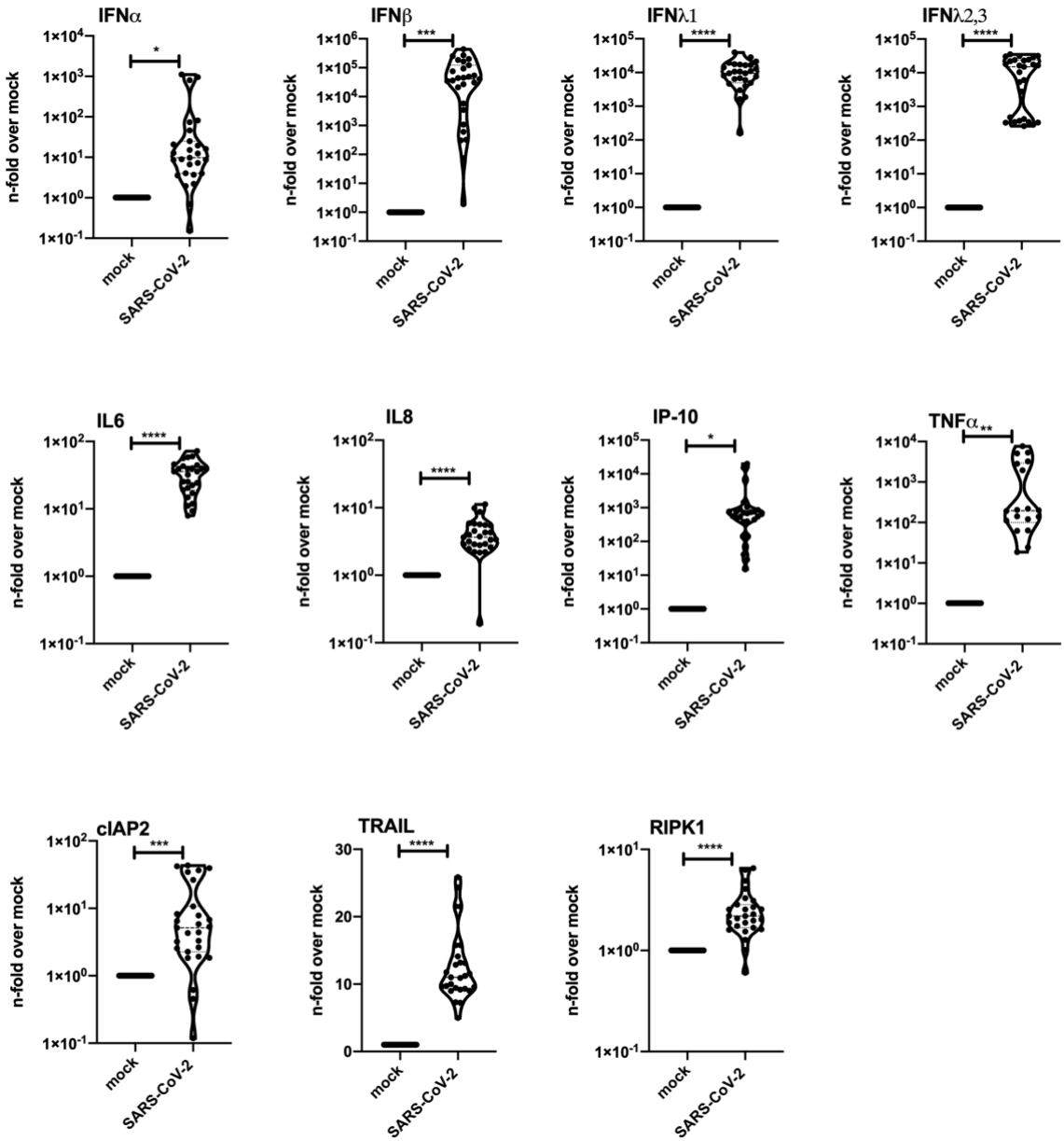

802

803

Figure 4

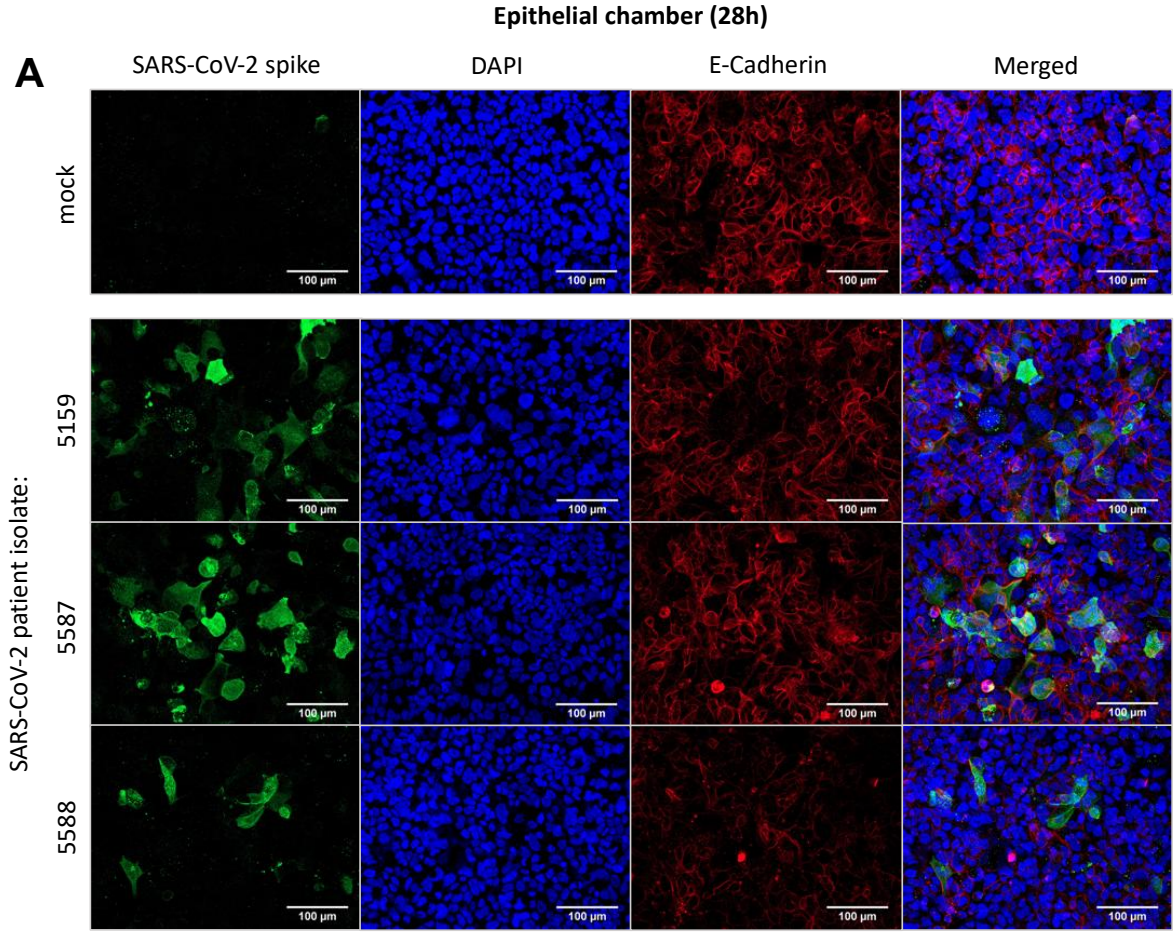

804

805

Figure 4

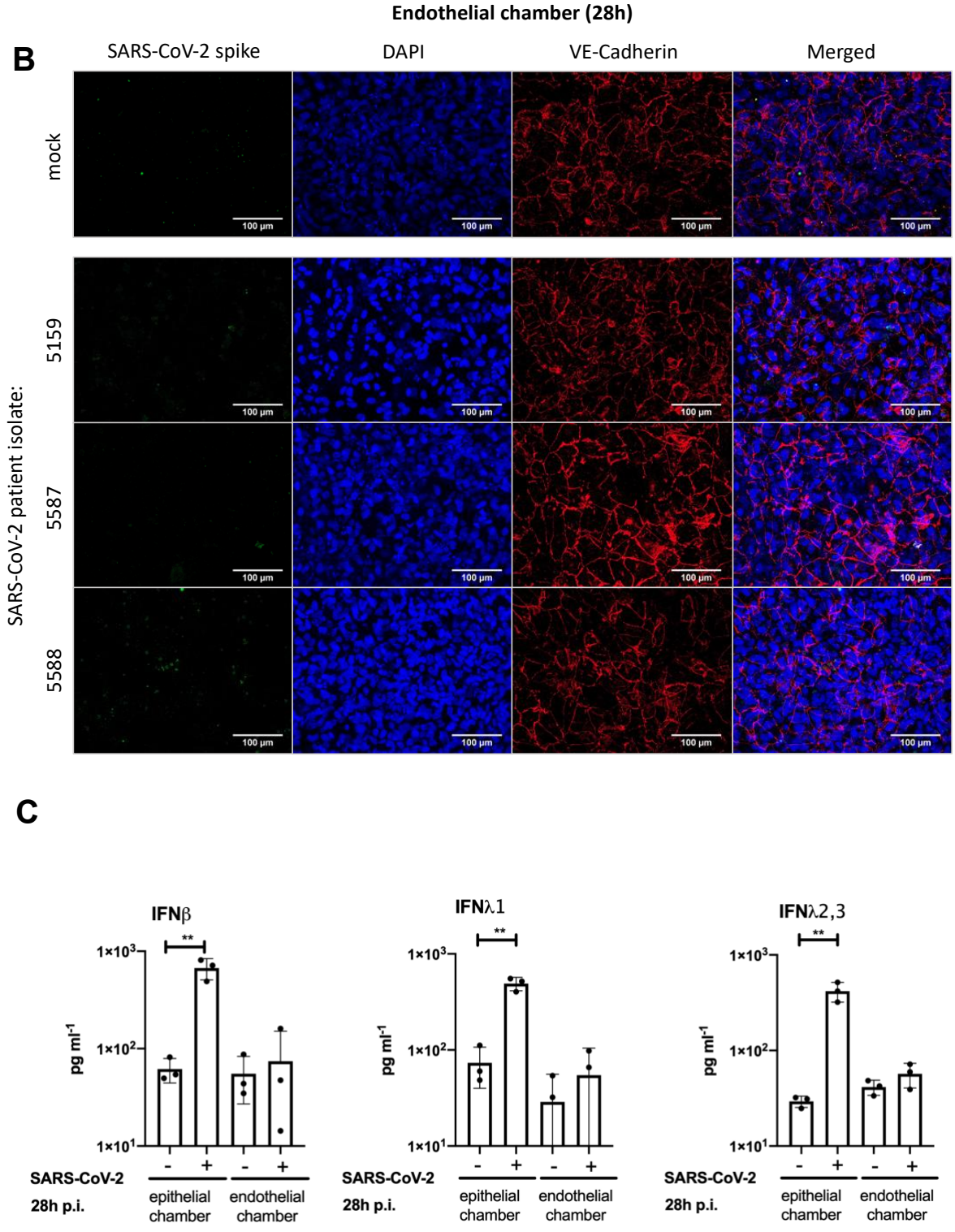

806

807

Figure 5

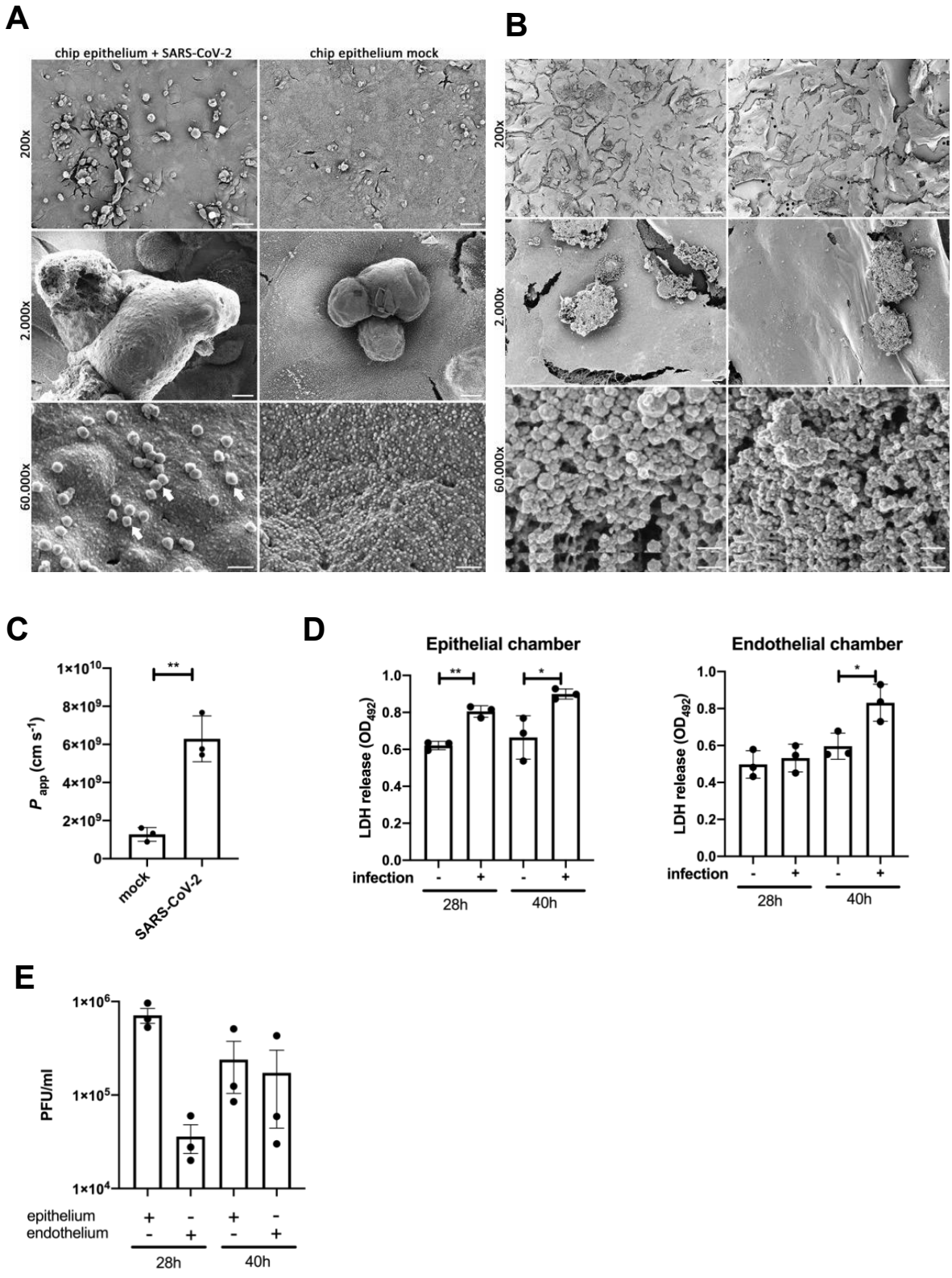

808

809

Figure S1

A

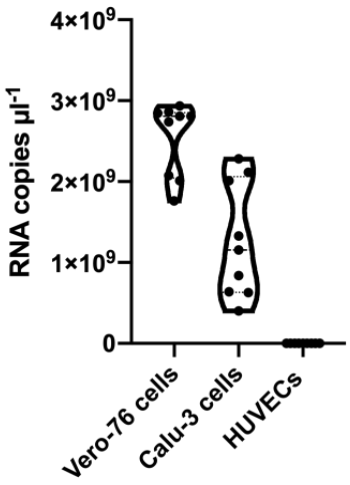

B

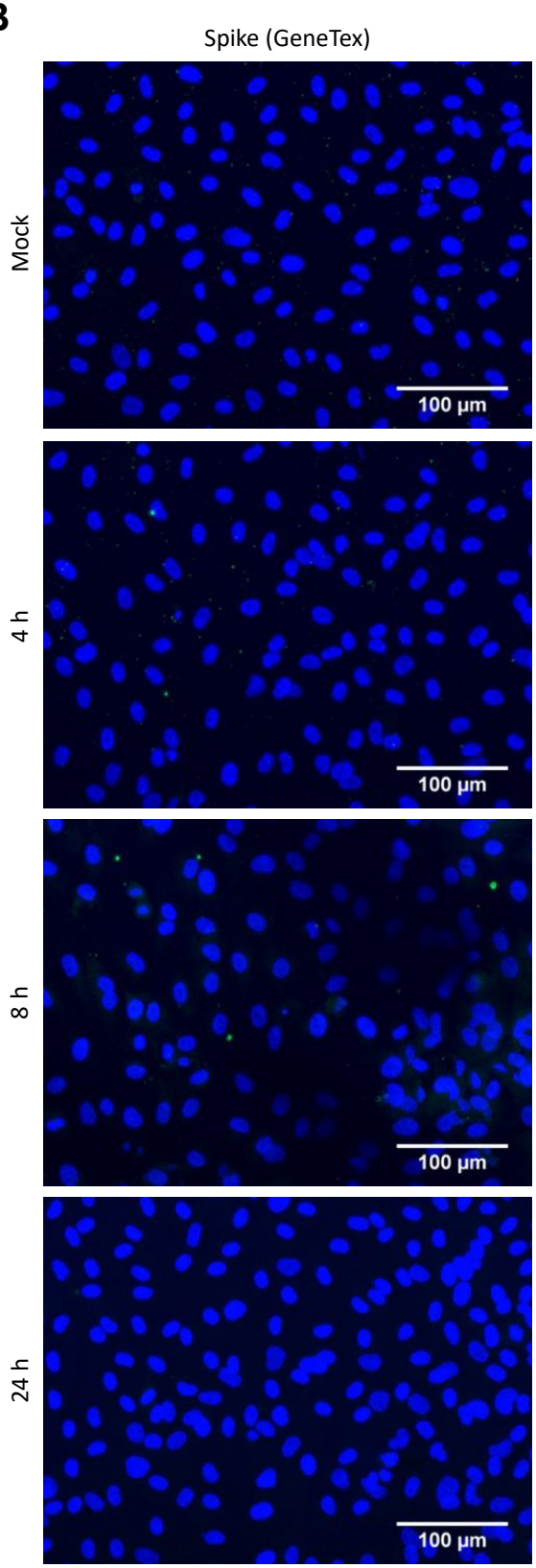

SARS-CoV-2 spike (green)
Nucleus (DAPI, blue)

812

813

Figure S2

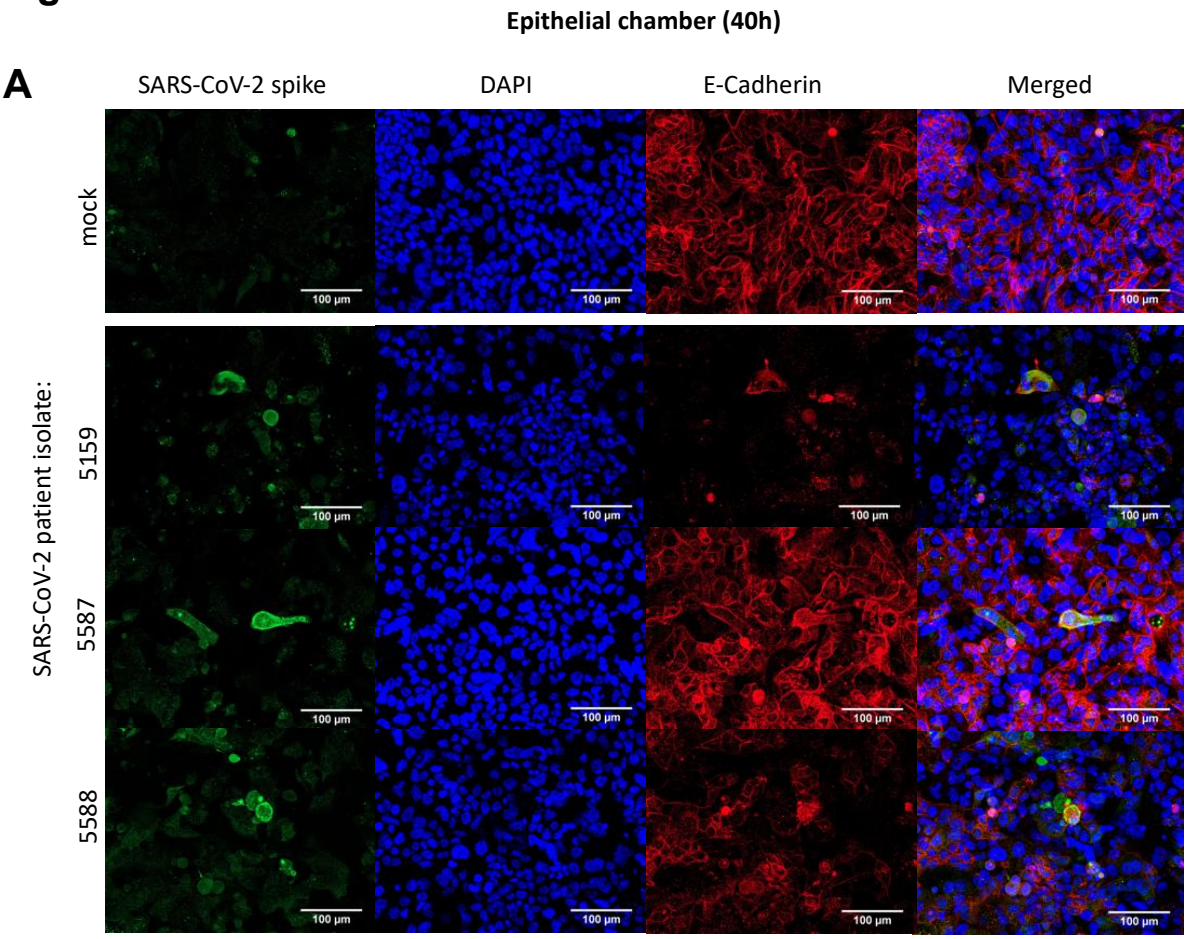

814

815

Figure S2

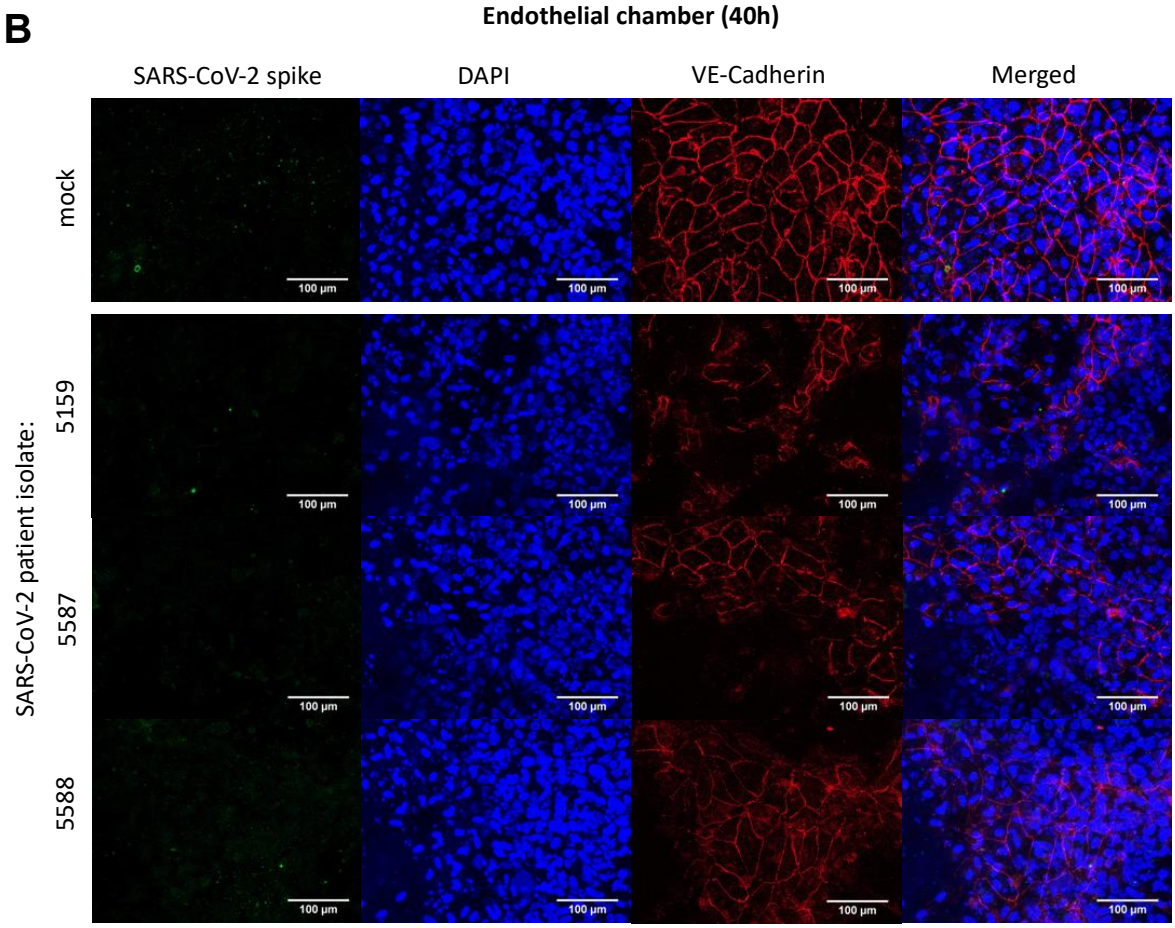

816

817

STAR ★ METHODS

KEY RESOURCES TABLES

REAGENT or RESOURCE	SOURCE	IDENTIFIER
Antibodies		
SARS-CoV-2 spike, mouse	GeneTex	GTX632604
E-Cadherin, rabbit	Cell Signaling	3195S
VE-Cadherin, rabbit	SinoBiological	2158S
ERK2, mouse	Santa Cruz	sc-1647
SARS-CoV-2/2019-nCoV Spike/S2 Rabbit Antibody	Sino Biological	40590-T62
Goat anti-Mouse IgG (H+L) Secondary Antibody, HRP	BIORad	31430
goat-anti-rabbit-igg-h-l-hrp-conjugate	BIORad	1706515
AF488, secondary antibody	Dianova	115-545-146
Cy5, secondary antibody	Dianova	111-175-144
Alpha-Tubulin, Rabbit	Cell signaling Technology	2144S
Cell lines		
Vero-76	ATCC	CRL 1587
Calu-3	ATCC	HTB-55
Chemicals		
RPMI 1640	Lonza	BE12-115F
EMEM	Sigma Aldrich	M7278
M199	Lonza	BE12-117F
Fetal serum	Sigma Aldrich	F7524
Human serum	Sigma Aldrich	H4522
10x MEM for plaque assay medium	Gibco	21430
Endothelial growth supplement (ECGS)	Sigma	02-102
Hoechst 33342	Merck	14533
Commercial Kits		
CyQUANT LDH cytotoxicity assay kit	Thermo Fisher Scientific	C20301
RNeasy Mini Kit	Qiagen	74106
QIAmp viral RNA Mini Kit	Qiagen	52906
RIDA Gene SARS-CoV-2 real-time PCR kit	R-Biopharm	PG6815
Legendplex Human anti-virus response panel kit	Biolegend	740349
Oligonucleotides		
human_IP-10_fw 5′-CCAGAATCGAAGGCCATCAA-3′	metabion	N/A
human_IP-10_rev 5′-TTTCCTTGCTAACTGCTTTCAG-3′	metabion	N/A
human_TNF-alpha_fw 5′-GGAGAAGGGTGACCGACTCA-3′	metabion	N/A
human_TNF-alpha_rev 5′-CTGCCCAGACTCGGCAA-3′	metabion	N/A
human_IFNβ_fwd 5′-TCTGGCACAACAGGTAGTAGGC-3′	metabion	N/A

human_IFNβ_rev 5′-GAGAAGCACAACAGGAGAGCAA-3′	metabion	N/A
human_GAPDH_fw 5′-CTCTGCTCCTCCTGTTCGAC-3′	metabion	N/A
human_GAPDH_rev 5′-CAATACGACCAAATCCGTTGAC-3′	metabion	N/A
C_GAPDH_fwd 5′-ACACCCACTCTTCCACCTTC-3′	metabion	N/A
C_ GAPDH_rev 5′-CTCTCTCTTCCTCTTGTGCTC-3′	metabion	N/A
human_IP-10_fw 5′-CCAGAATCGAAGGCCATCAA-3′	metabion	N/A
Software		
Zen, 2.6 (blue edition)	Carl Zeiss AG	N/A
MrBayes	v3.2	N/A
Systems for cDNA Synthesis and qRT-PCR		
Nano-Drop	Nano-Drop 1000 (PEQLAB Biotechnology GmbH)	N/A
Thermo cycler (for cDNA synthesis)	Peqstar (PEQLAB Biotechnology GmbH)	N/A
Realtime PCR cycler	Rotor Gene Q (QIAGEN)	N/A
Acquisition software for RNA concentration	NanoDrop 1000 V3.8.1 (ThermoFisher Scientific)	N/A
Acquisition software for qRT-PCR	Q-Rex V1.1.0.4 (QIAGEN)	N/A
Software used for subsequent data analysis	Microsoft Office 2010 (Microsoft) GraphPad Prism V8.3.0.538 (Graphpad Software, Inc.)	N/A
Systems for microscopy		N/A
Model	Carl Zeiss Observer.Z1	N/A
Type of objective lenses	Plan-Apochromat	N/A
Magnification of objective lenses	20x	N/A
Numercial aperture of objective lenses	0.8	N/A
Imaging medium	Dako Fluorescence Mounting Medium	N/A

camera	Zeiss Axioxam 503 mono	N/A
ApoTome	ApoTome.2 Carl Zeiss	N/A
Aquisition software	Zeiss Zen 2.6 (blue edition)	N/A
Operations involved (deconvolution, Fourier-Filter, gamma)	Deconvolution, gamma correction, phase error correction	N/A
File formats	16-bit	N/A
Sample Preparation, Sequencing and Analysis		
MinION - Sequencer	Oxford Nanopore Technologies	N/A
Ligation Sequencing Kit (SQK-LSK109)	Oxford Nanopore Technologies	N/A
R9.4.1 flow cells Nanopore FLO-MIN106	Oxford Nanopore Technologies	N/A
Native Barcoding Expansion (EXP-NBD104)	Oxford Nanopore Technologies	N/A
Workflow: poreCov via nextflow using docker	For genome reconstruction (version 0.2)	https://github.com/replikation/poreCov
Primer Scheme V3 was used for amplicon-based sequencing of SARS-CoV-2	V3	https://github.com/artic-network/artic-ncov2019/blob/master/primer_schemes/nCoV-2019/V3/nCoV-2019.tsv
NEBNext Ultra II End-prep	NEB	M0493S
NEBNext Quick Ligation Module	NEB	E6056S
Q5 Hot Start HF Polymerase	NEB	M0493S
RNase OUT (125 rxn)	Thermofischer	10777019
Random Hexamers (50 μM)	Thermofischer	N8080127
Zymo Quick-RNA Viral Kit	Zymo	R1034
SuperScript IV (50 rxn)	Thermofischer	18090050
dNTP mix (10 mM each)	Thermofischer	R0192